

This is a preprint of the following article, which is available at: <http://mdolab.engin.umich.edu>  
Y. Liao, J. R. R. A. Martins and Y. L. Young. Sweep and Anisotropy Effects on the Viscous Hydroelastic Response of Composite Hydrofoils. *Composite Structures*, Vol.230, No. 111471, December 2019.

The original article may differ from this preprint and is available at:  
<https://doi.org/10.1016/j.compstruct.2019.111471>.

# Sweep and Anisotropy Effects on the Viscous Hydroelastic Response of Composite Hydrofoils

Yingqian Liao, Joaquim R. R. A. Martins and Yin L. Young  
*University of Michigan, Ann Arbor, MI, 48109*

## Abstract

Composite materials have become prevalent in hydrofoil design due to their favorable characteristics. Both material anisotropy and planform sweep are factors that affect hydrofoil performance. However, the interplay between these two factors has not been studied systematically. This paper investigates this interplay in the viscous hydroelastic response of linearly tapered composite hydrofoils with a modified NACA 0009 cross-section using high-fidelity hydrostructural simulations. The simulations are based on a Reynolds-averaged Navier–Stokes solver coupled to a structural finite–element model. Both sweep and off-axial fiber layup reduce the bending-mode natural frequencies due to the decrease in bending rigidity. Sweep reduces the form drag by suppressing trailing edge separation, but it can increase the lift-induced drag by causing the spanwise load distribution to deviate away from the ideal elliptical distribution. The spanwise load distribution can be tailored to reduce the induced drag and delay cavitation inception using sweep-induced geometric, material-induced bend-twist coupling, or both. Nevertheless, a poor combination of sweep and material configurations can cause static divergence, early separation, cavitation, noise, and material failures. Besides changing the structural response and resultant fluid-structure interaction, the material failure inception load and failure location depend directly on the fiber orientation due to the anisotropic characteristic of composites.

## 1 Introduction

The increasingly stringent efficiency requirements and demands of maritime transport and ocean energy have motivated innovative means to improve the performance of maritime structures. Marine lifting surfaces, such as marine propulsors, tidal turbines, and

control surfaces, are critical parts of maritime platforms that affect the overall system performance. Recently, advances in material science, manufacturing techniques, and innovative design methodologies have enabled the production of sophisticated geometries and new materials to improve the performance of marine lifting surfaces [1].

Marine lifting surfaces are usually swept to improve the performance or to achieve specific functions, such as delaying cavitation and stall, reducing unsteady load fluctuations and induced pressure pulses on the hull, and avoiding entanglement with underwater debris. Cavitation involves phase change from liquid to vapor when the local pressure drops to near the saturated vapor pressure of the fluid, and can lead to undesirable effects, such as performance decay, noise, vibration, and cavity-induced erosion [1].

Sweep changes the hydrodynamic performance of lifting surfaces by changing the effective inflow velocity and the spanwise loading distribution through upwash and downwash [2]. Hodges and Pierce [3, 4.2.6] illustrated the sweep effect on the aeroelastic characteristics. Sweep changes the effective streamwise angle of attack when the lifting surface bends, which couples the spanwise bending and torsion deformations. This sweep-induced geometric bend-twist coupling complicates the static hydroelastic response, as well as the vibration and noise characteristics of marine lifting surfaces.

In marine propulsors, sweep is usually referred to as *skew*. Many marine propulsors are designed with highly skewed blades to delay the cavitation and alleviate the unsteady load fluctuations on the propeller blades, shaft, and hull surfaces caused by spatially varying inflow caused by hull-propulsor-rudder interactions and by shaft inclination. Experimental hydrofoil results by Ihara et al. [4] show that partial cavitation-induced oscillations were attenuated with increased sweep angle. Cumming et al. [5] also found that increasing skew lead to decreased unsteady thrust and torque fluctuations, and delayed cavitation inception for marine propellers. Sweep can also cause a secondary flow and change the spanwise cavity shape and shedding frequency [4, 6].

Composite materials have a high strength-to-weight ratio, improved damping, better fatigue performance, and lower maintenance cost relative to metallic alloys [1, 7]. In addition, material-induced bend-twist coupling can be introduced by tailoring the composite layups. Well-designed composite marine lifting surfaces can increase the efficiency, and delay cavitation, separation, and stall [8–10].

Recent research efforts have improved the understanding of the effects of sweep and material anisotropy on the performance of hydrodynamic lifting surfaces, but not much work has been focused on the interplay between these two factors. More thorough investigations on this interplay have been done in aircraft wings [11–15]. The propensity of forward-swept wings to static divergence can be prevented by tailoring the composite layup [11]. Weisshaar et al. [14, 15] demonstrated that the bend-twist coupling induced by material anisotropy can counteract the undesirable characteristics of forward-swept wings, and discussed the influence of elastic tailoring on the spanwise center of pressure and lateral control effectiveness.

The considerations in designing marine lifting surfaces differ from aircraft wings because of the different governing physics, such as the strong hydrodynamic added mass, damping, and disturbing force effects caused by the much higher water density, as well as potential susceptibility to cavitation, ventilation, and wave loads [1, 16–21].

Because of the added mass effect in water, marine lifting surfaces have lower system resonance frequencies, and the resonance frequencies and damping coefficients exhibit speed dependency at much lower speeds than in air [19, 22–26].

Moreover, as shown in the numerical work of Akcabay and Young [22] and experiment work of Besch and Liu [27], a new mode with frequencies much lower than the structural modes (modes that exist in quiescent fluid) can emerge at high speeds, and can cause early and unexpected divergence. The new mode is caused by changes in the system damping and stiffness by the circulatory terms in the fluid forces that are proportional to the fluid density, so the new mode emerges at much lower speeds in water compared to in air. In addition, Akcabay and Young [22, 23] found that lightweight composite hydrofoils tend to be more susceptible to single-mode flutter, caused by the damping of the new low-frequency mode going to zero, rather than the coupled mode flutter more typical of airfoils.

Recently, there have been a number of numerical studies on the response of composite marine lifting surfaces. Coupled boundary element methods and finite element methods have gained popularity because of their computational efficiency and ability to capture important fluid and structure interaction features [8–10, 28–31]. However, potential flow solvers, such as boundary element methods, cannot predict viscous flow phenomena, such as separation and stall. Considering these viscous effects is critical to hydrodynamic lifting surface response prediction, especially when the flexibility increases and when operating in off-design conditions. This increased flexibility can result in different deformed shapes that change the spanwise load distribution, which affects the separation onset and locations, cavitation and stall inception, as well as structural stress distributions and flow-induced vibration frequencies. Once separation and stall occur, the hydrodynamic efficiency drops significantly and the associated instabilities can cause structural failure. High-fidelity simulations are needed in lifting surface design to capture separation, cavitation inception, vortex generation and shedding, as well as material failure.

Garg et al. [32] developed a high-fidelity framework that couples a Reynolds-averaged Navier–Stokes (RANS) solver and a finite element method (FEM) solver to optimize metallic hydrofoils. The performance of the baseline hydrofoil and a hydrofoil optimized using this framework has been validated by experiments [33]. Liao et al. [34] extended this framework’s ability to predict the hydroelastic response of composite hydrofoils by implementing a composite solid element module. Contrary to typical composite aircraft wings, which use thin-shell type structures with hollow or foam cores, marine composite lifting surfaces typically require solid structures because of the high fluid loading owing to the high water density. Hence, solid elements are needed to model the thicker solid composite structures. This framework, called MACH (multidisciplinary design optimization of aircraft configurations with high-fidelity), was initially intended for aircraft wing design and leverages gradient-based optimization and coupled adjoint derivative computation to enable the optimization with respect to many design variables [35–37].

Our eventual goal is to use MACH to design composite hydrodynamic lifting surfaces considering materials selection and ply layup, as well as geometric parameters including shape and planform variables. However, we first need to understand the in-

interaction between sweep and material anisotropy in viscous flow, so that we can gain insights for our design optimization studies. To achieve this objective, the main tasks of this paper are to investigate how the following hydrofoil characteristics are affected by sweep and material anisotropy: 1) in-vacuo free vibration characteristics; 2) hydroelastic response; 3) separation, stall, and static divergence behavior; 4) investigate the cavitation inception and vortex structure; 5) susceptibility to material failure.

## 2 Methodology

In this section, we briefly overview the framework used for the numerical simulations, and introduce the model dimensions and key definitions. We also describe the chosen sample configurations used in our analysis and the simulated condition.

### 2.1 Numerical Framework

The MACH framework couples a high-fidelity CFD solver a high-fidelity FEM solver to predict the hydroelastic response and to perform the simultaneously design optimization of the hydrodynamic shape and the structure.

The CFD solver in MACH is ADflow<sup>1</sup> (open source), which solves Euler, laminar Navier–Stokes, and RANS equations on multiblock and overset meshes with a second-order finite volume scheme [38]. A discrete adjoint method implementation enables ADflow to efficiently compute sensitivities with respect to a large number of variables [38, 39]. To investigate viscous effects, we solve the RANS equations with Spalart–Allmaras turbulence model. The solution process starts with an approximate Newton–Krylov method, and then switches to an exact Newton–Krylov method to converge to a required tolerance [40].

The structural solver is TACS (Toolkit for the Analysis of Composite Structures), which was initially developed to solve ill-conditioned thin-shell problems typical in aircraft structures [41]. Garg et al. [32] extended TACS to handle solid elements, which are required for marine structures, and Liao et al. [34] added and verified an orthotropic solid element implementation.

The coupled hydroelastic solution is achieved using a block Gauss–Seidel iteration. From the flow solution, hydrodynamic loads are evaluated and transferred to the structure using the method of virtual work [35]. The external loads displace the structure, which in turn perturbs the CFD mesh. The movement of surface mesh is determined by extrapolating the structural displacements through rigid links [35, 42] and these displacements propagate to the volume mesh using an inverse distance weighting mesh deformation algorithm [43].

### 2.2 Hydrofoil Model

We generate simple hydrofoil models with a linear taper and a modified NACA 0009 cross-section for our studies. The hydrofoils have the same geometry as previous experimental studies [1, 44], but varying linear sweep is added, and the material is simplified

---

<sup>1</sup><https://github.com/mdolab/adflow>

as uni-directional carbon fiber reinforced polymers (CFRP) to study the interplay between fiber angle and sweep. The hydrofoils have a root chord of 0.12 m and a semi-span of 0.3 m. The sweep ( $\lambda$ ) is defined as the angle between the mid-chord axis and the global  $y$ -axis. The fiber angle ( $\theta_f$ ) is defined as the angle between the fiber longitudinal direction and the mid-chord axis, as shown in Figure 1. The sweep angle is positive when swept backward. The fiber angle is positive when swept forward. The flow velocity is aligned with the  $x$  direction and positive, as shown by the arrows in Figure 1.

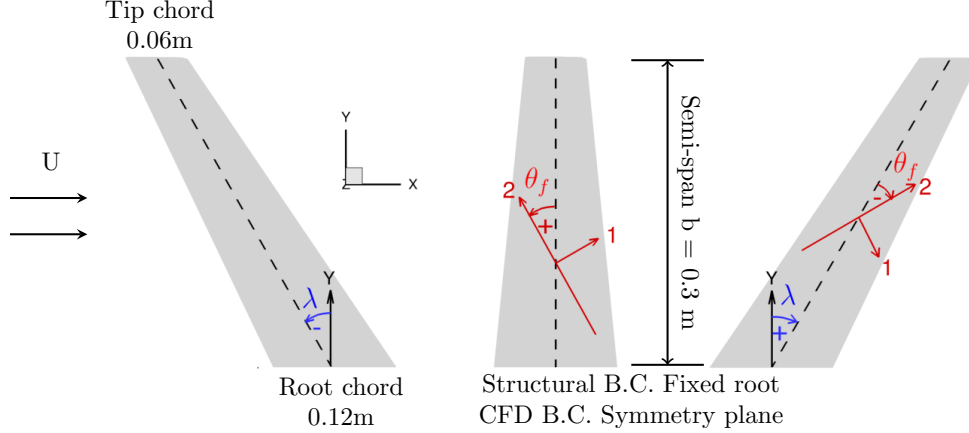


Figure 1: Definition of sweep ( $\lambda$ ) and fiber angle ( $\theta_f$ ). The sweep angle is defined positive when swept backward. The fiber angle is defined positive when swept forward. Dashed lines represent the mid-chord axis. The material coordinates are shown in red.

Consistent mesh sizes are used for hydrofoils with different sweeps. A mesh convergence study is shown later, in Section 3.1. Previous efforts have validated the CFD solver against experimental results [32, 33] and the composite solid element in the FEM solver has been verified against the commercial FEM software ABAQUS [34]. Examples of the CFD and FEM meshes of the unswept hydrofoils used in the hydrostructural simulation are shown in Figure 2. The CFD mesh has 10,222,080 cells and a maximum  $y^+ = 0.4$ , while the FEM mesh has 121,200 8-node brick elements.

The material anisotropy is modeled with orthotropic solid elements using the properties of uni-directional CFRP. The material properties are listed in Table 1. For stainless steel hydrofoils, we use stainless steel 316 properties, which are listed in Table 2.

## 2.3 Hydrofoil Features, Flow Conditions, and Post-processing

We conducted a series of modal analyses and hydrostructural simulations for nine hydrofoils featuring different sweep angles ( $+30^\circ$ ,  $0^\circ$ , and  $-30^\circ$ ) and different materials (stainless steel, CFRP  $+30^\circ$ , CFRP  $-30^\circ$ ) to compare the performance. The sweep angles and fiber angles chosen here might not be practical or optimal; they are chosen to provide greatly simplified examples to show the fundamental differences in performance. To avoid confusion in the terms that refer to hydrofoils, we use “forward”

Table 1: CFRP material properties, where the 1, 2, and 3 directions represent the Cartesian coordinates defined with respect to the fiber axis, as shown in Figure 1.

Symbol	Description	Value	Units
$\rho_s$	Solid density	1590	kg/m <sup>3</sup>
$E_1, E_3$	Young's modulus	13.40	GPa
$E_2$	Young's modulus	117.80	GPa
$G_{12}, G_{23}$	Shear modulus	3.90	GPa
$\nu_{21}, \nu_{23}$	Poisson's ratio	0.25	–
$\nu_{13}$	Poisson's ratio	0.45	–
$X_T, Z_T$	Transverse tensile strength	81	MPa
$X_C, Z_C$	Transverse compressive strength	250	MPa
$S_{12}, S_{23}$	Shear strength	136	MPa
$S_{13}$	Shear strength	50	MPa

Table 2: Stainless steel 316 material properties.

Symbol	Description	Value	Units
$\rho_s$	Solid density	7870	kg/m <sup>3</sup>
$E$	Young's modulus	200	GPa
$\nu$	Poisson's ratio	0.27	–
$Y_S$	Yield strength	290	MPa



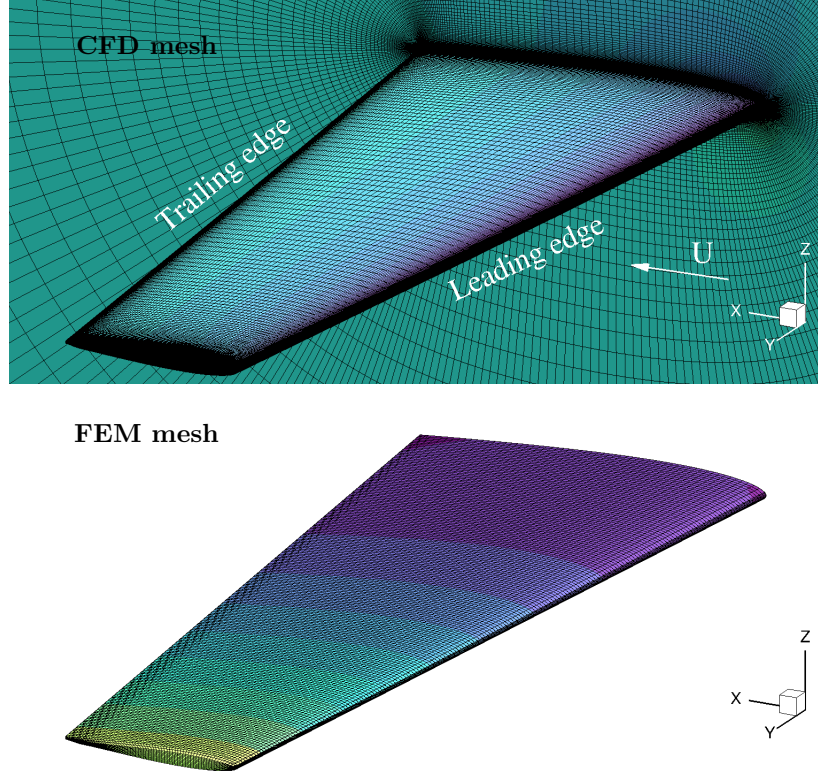


Figure 2: CFD and FEM meshes for the stainless steel unswept hydrofoil. The meshes for the forward- and backward-swept hydrofoils have the same size.

to indicate the hydrofoil with the negative sweep ( $\lambda = -30^\circ$ ), “unswept” for  $\lambda = 0^\circ$ , and “backward” for  $\lambda = +30^\circ$ , together with material configurations stainless steel, CFRP  $+30^\circ$  ( $\theta_f = +30^\circ$ ), and CFRP  $-30^\circ$  ( $\theta_f = -30^\circ$ ). In reality, lifting surfaces are required to sustain a given design load, so all the hydroelastic responses shown in results section are compared at the same lift coefficient  $C_L = 0.65$  except where noted. A fixed Reynolds number of  $10^6$  (mean-chord based) is used in all hydrostructural simulations. The  $\lambda_2$  criterion is computed using a Tecplot add-on and the tensor eigensystem tool in Tecplot. Some observations are limited to the hydrofoil model used in this study, but the explanations and the underlying physics should be generally applicable for most marine lifting surfaces.

## 3 Verification

### 3.1 CFD Mesh Convergence

To compare the performance of different hydrofoils, it is important to use CFD meshes that converge to a small tolerance and to the same level for different geometries. We

compared the predicted  $C_L$  and  $C_D$  values from hydrodynamic-only simulations at angle of attack  $\alpha = 4^\circ$  for five meshes with different sizes, ranging from 403,200 to 25,804,800 cells for three hydrofoils with different sweeps, as shown in Table 3. The  $C_D$  value for the mesh with about 10 million cells (L1) differs from the finest mesh (L0) by less than  $10^{-4}$  and the largest  $C_L$  difference is only 0.4%, so we use the L1 CFD mesh for all our hydrostructural simulations.

Mesh	Level	Mesh size	$y_{\max}^+$	$C_L$	$C_D$
Unswapt	L0	25,804,800	0.26	0.32769	<u>0.01864</u>
	L1	10,222,080	0.35	0.32841	<u>0.01876</u>
	L2	3,225,600	0.53	0.32970	0.02021
	L3	1,277,760	0.74	0.33057	0.02194
	L4	403,200	1.10	0.33163	0.02609
Forward	L0	25,804,800	0.27	0.29270	<u>0.01666</u>
	L1	10,222,080	0.37	0.29400	<u>0.01668</u>
	L2	3,225,600	0.56	0.29577	0.01786
	L3	1,277,760	0.78	0.29717	0.01934
	L4	403,200	1.10	0.29928	0.02272
Backward	L0	25,804,800	0.24	0.30377	<u>0.01742</u>
	L1	10,222,080	0.40	0.30377	<u>0.01742</u>
	L2	3,225,600	0.53	0.30475	0.01869
	L3	1,277,760	0.72	0.30497	0.02027
	L4	403,200	1.30	0.30386	0.02397

Table 3: Based on the CFD convergence study (hydrodynamic only,  $\alpha = 4^\circ$ ), we chose the L1 mesh for our hydrostructural simulations.

### 3.2 FEM Mesh Convergence

We used modal analysis to assess the convergence of the structural meshes. We compared the first two in-vacuo natural frequencies of three different mesh sizes for three CFRP  $-30^\circ$  hydrofoils with different sweep values. The natural frequency comparison is shown in Table 4. For the first in-vacuo natural frequencies, the largest discrepancy between L0 and L1 meshes is only 0.6% (backward case), and this discrepancy decreases to 0.3% between L1 and L2 meshes. For the second in-vacuo natural frequencies, the largest discrepancy between L1 and L2 meshes is only 0.4% (backward case). As a result, we select the L1 FEM mesh with 121,200 elements for all our hydrostructural simulations.

## 4 Results

In this section, we first examine the influence of sweep and material anisotropy on the natural frequencies and mode shapes obtained from modal analysis. We then compare the steady-state hydroelastic response of stainless steel, CFRP  $+30^\circ$ , and CFRP  $-30^\circ$



Mesh	Level	Mesh size	Mode 1 (Hz)	Mode 2 (Hz)
Unswept	L0	62,208	85.391	357.461
	L1	121,200	85.139	356.221
	L2	210,816	84.998	355.516
Forward	L0	62,208	67.607	287.408
	L1	121,200	67.284	285.702
	L2	210,816	67.104	284.743
Backward	L0	62,208	58.162	246.781
	L1	121,200	57.813	245.045
	L2	210,816	57.619	244.079

Table 4: First two in-vacuo natural frequencies of CFRP  $-30^\circ$  hydrofoils. Based on the FEM convergence study, we chose the L1 FEM mesh for our hydrostructural simulations.

hydrofoils for three sweep configurations at the same lift condition ( $C_L = 0.65$ ) to investigate how sweep and material anisotropy affect the loading, flow streamlines and pressure distributions, deformation patterns, as well as the resultant forces and efficiency. Since cavitation is related to low pressure coefficient ( $C_p$ ) that drops to saturated vapor pressure on the lifting surface, sectional  $C_p$  curves are shown to compare the susceptibility to cavitation. We also discuss the vortex structure based on iso-surfaces of the  $\lambda_2$  criterion, since strong vortices can cause severe noise or vibration issues. Finally, we show the matrix compressive/tensile cracking index contours to assess the influence of sweep and material anisotropy on susceptibility to structural failure.

## 4.1 Modal Analysis

The modal analysis computes in-vacuo natural frequencies and mode shapes, which are related to structural mass and stiffness, and can be used to predict the structural response. Additionally, we want to understand the influence of sweep and material anisotropy on the natural frequencies and mode shapes to avoid dynamic load amplification and vibrations in a real design. This is especially important for hydrodynamic lifting surfaces, where the vibration characteristics can be further complicated by hydrodynamic added mass effects, as well as speed- and frequency-dependent hydrodynamic damping and de-stiffening effects [18, 19, 22–26].

The first and second modes of all the stainless steel hydrofoils presented here are bending-dominated modes because the structural spanwise dimension (structural span) is larger than the chordwise dimension, and the hydrofoils are cantilevered at the root. Based on the first modes of stainless steel hydrofoils, these three hydrofoils primarily undergo pure bending when observed along the structural span.

As shown in Figure 3, sweep reduces the natural frequencies due to the extended structural span. This reduction is more significant for the bending-dominated modes than for the twist-dominated modes. The bending rigidity of the forward stainless steel

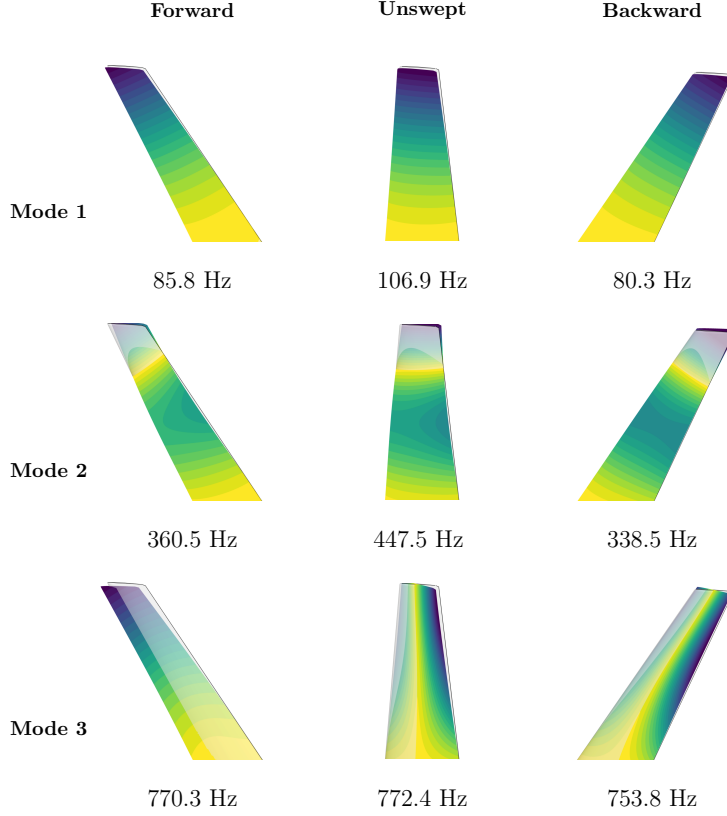


Figure 3: First three in-vacuo modes and natural frequencies of stainless steel hydrofoils with different sweep angles. Sweep decreases the natural frequencies because of the extended structural span. The light gray shape indicates the undeformed geometry, while the color contours of displacement magnitude are shown on the deformed geometry.

hydrofoil is decreased to the extent that its third mode is an in-plane bending mode, while the third modes for the unswept and backward hydrofoils are twist-dominated. This difference in the third mode between forward hydrofoils and backward hydrofoils is caused by the asymmetry about the mid-chord of the NACA 0009 cross-section.

The bending mode natural frequencies are further reduced in water due to the added mass effect, particularly for lightweight composite structures that have a lower solid-to-fluid density ratio. The bending mode frequencies are expected to decrease more than the twisting mode frequencies underwater because the added mass effect is dependent on the direction of the movement, and bending motions move a higher volume of surrounding fluid. Therefore, sweep changes the susceptibility to mode switching, since the gap between a bending mode frequency and an adjacent twisting mode frequency varies with sweep [16, 45].

Comparing Figures 3–5, we see that off-axis fiber layup further decreases the bending rigidity compared to stainless steel hydrofoils, which reduces the natural frequencies of the bending-dominated modes. For backward hydrofoils, CFRP  $-30^\circ$  and

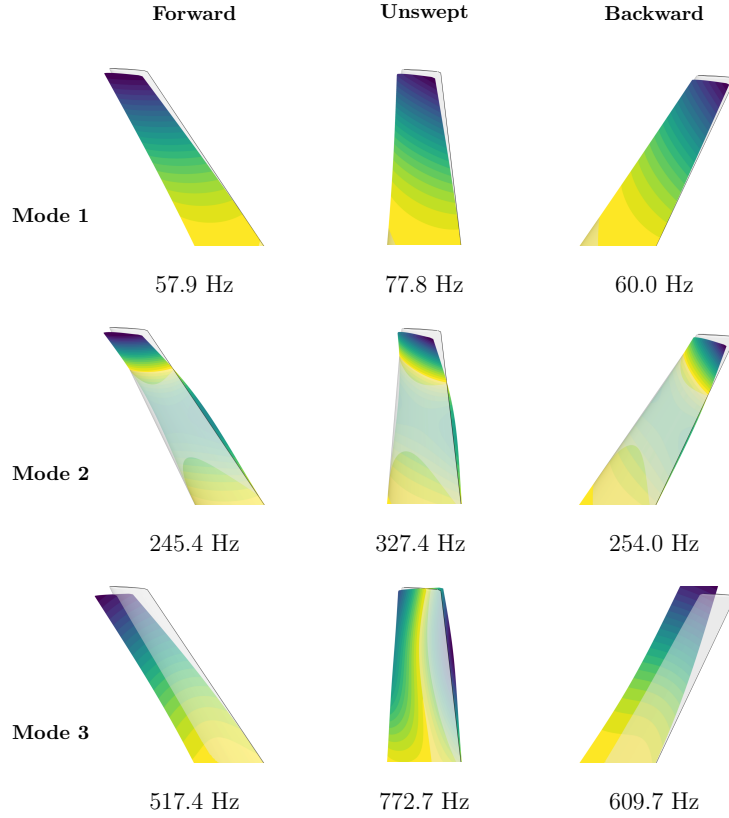


Figure 4: First three in-vacuo modes and natural frequencies of CFRP +30° hydrofoils with different sweep angles. The off-axis fiber layup decreases the natural frequencies. The light gray shape indicates the undeformed geometry, while the color contours of displacement magnitude are shown on the deformed geometry.

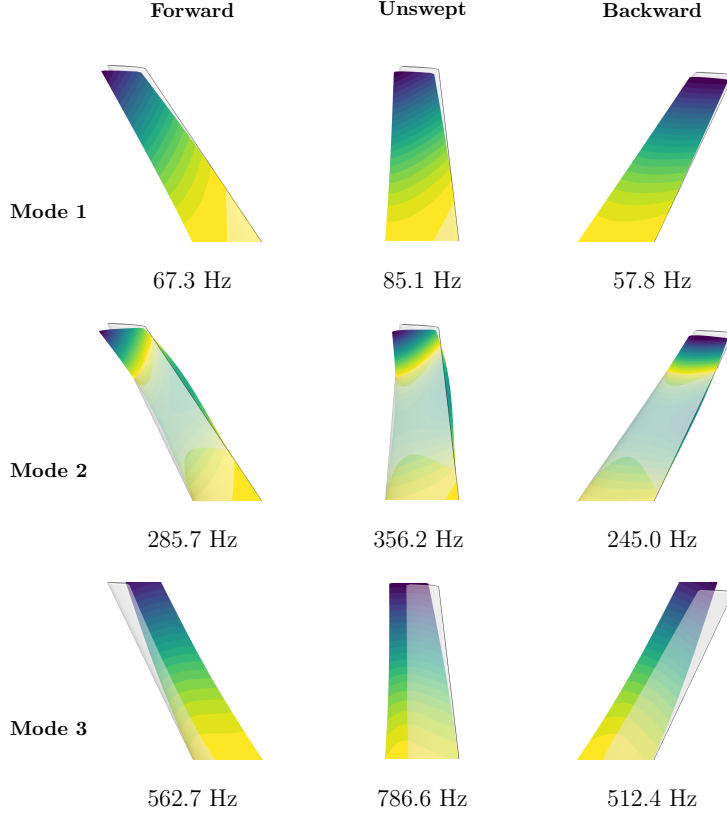


Figure 5: First three in-vacuo modes and natural frequencies of CFRP  $-30^\circ$  hydrofoils with different sweep angles. The off-axis fiber layup decreases the natural frequencies. The light gray shape indicates the undeformed geometry, while the color contours of displacement magnitude are shown on the deformed geometry.

CFRP  $+30^\circ$  change the third mode from twisting-dominated to bending-dominated compared to the stainless steel hydrofoil because of the lower bending stiffness. Similarly, for unswept hydrofoils, the CFRP  $-30^\circ$  hydrofoil has a bending-dominated third mode while the stainless steel hydrofoil has a twisting-dominated third mode. The corresponding in-water natural frequencies and modes can be significantly different from stainless steel hydrofoils due to the direction-dependency of the added mass. Additionally, the damping coefficient in water, which is related to the modes, also impacts the vibration behavior of hydrodynamic lifting surfaces [18, 19, 22–26].

## 4.2 Steady-state Hydroelastic Response

The modal analysis has shown the effect of sweep and material anisotropy on the structural stiffness, which can affect the hydroelastic response. To understand the influence of sweep and material isotropy on the hydroelastic response, we compare the hydrostructural simulation results of different hydrofoils at the same loading condition ( $C_L = 0.65$ ), as shown in Figure 6. The comparison includes the hydrodynamic efficiency (lift-to-drag ratio), tip twist angle  $\theta_{\text{tip}}$ , pressure contours, streamlines, spanwise

sectional lift coefficient  $C_l$ , and normalized lift distributions. The spanwise  $C_l$  distribution is the sectional lift coefficient along the span, while normalized lift distribution is the lift per unit length along the span.

We first compare results of hydrostructural simulations of the stainless steel hydrofoils, and then results of the composite hydrofoils with different fiber orientation and sweep angles to demonstrate the interaction between sweep and material anisotropy. All hydrofoils shown here bend up (towards the suction side) for all cases when the lift is positive.

#### 4.2.1 Influence of Sweep

The effects of sweep can be discussed based on the hydroelastic responses of the stainless steel hydrofoils, which are shown in the first row in Figure 6. According to the angle of attack ( $\alpha$ ) values listed under each hydrofoil in Figure 6, the required  $\alpha$  to achieve  $C_L = 0.65$  is higher for both swept hydrofoils than for the unswept hydrofoil because the effective inflow velocity and the effective incidence are reduced for swept hydrofoils.

Sweep changes the spanwise lift distribution through the vorticity-induced downwash and upwash effects. Forward sweep causes more downwash outboard and more upwash inboard, while backward sweep causes more downwash inboard and more upwash outboard [46, Sec. 9.3.4.3] [2, Sec. 8]. The  $C_l$  distribution in first row of Figure 6 shows that backward sweep decreases the  $C_l$  at the root and increases the  $C_l$  near the tip, while the forward hydrofoil exhibits the opposite trend, which suggests that the backward hydrofoil has a stronger tip vortex.

This  $C_l$  redistribution caused by the sweep is also evident from the  $C_p$  contours. For the forward stainless steel hydrofoil, the negative portion (suction peak, which could lead to cavitation) on the  $C_p$  contours is smaller at the tip compared to other spanwise stations, while the suction peak is smaller at the root for the backward stainless steel hydrofoil. Hence, backward sweep may increase the tendency of the hydrofoil to cavitate in the tip region, including tip vortex cavitation. Moreover, the backward hydrofoil is susceptible to the tip stall, while the forward hydrofoil is prone to the root stall. From the normalized lift distributions, the backward stainless steel hydrofoil has a higher bending moment because of the higher outboard loading.

From Figure 6, we see that the unswept stainless steel hydrofoil exhibits a lift distribution closer to elliptical than the other two swept hydrofoils. This suggests a lower lift-induced drag compared to the two swept hydrofoils, since an elliptical lift distribution leads to the lowest theoretical lift-induced drag for planar wakes.

However, from the stainless steel results shown in Figure 6, the total drag coefficient ( $C_D$ ) of the forward sweep hydrofoil decreases by 0.67% compared to the unswept hydrofoil, while sweeping the hydrofoil backward increases the drag by 0.62%. These changes in  $C_D$  are reflected in the efficiencies ( $C_L/C_D$ ), since  $C_L = 0.65$  for all the cases. These small drag differences are a result of both lift-induced drag and form drag. In spite of the low lift-induced drag, the form drag of the unswept hydrofoil is higher than the swept hydrofoils because of the more significant flow separation at the blunt trailing edge, so the total drag is close to that of the swept foils.

The unswept stainless steel hydrofoil has a pair of vortices that shed from the top

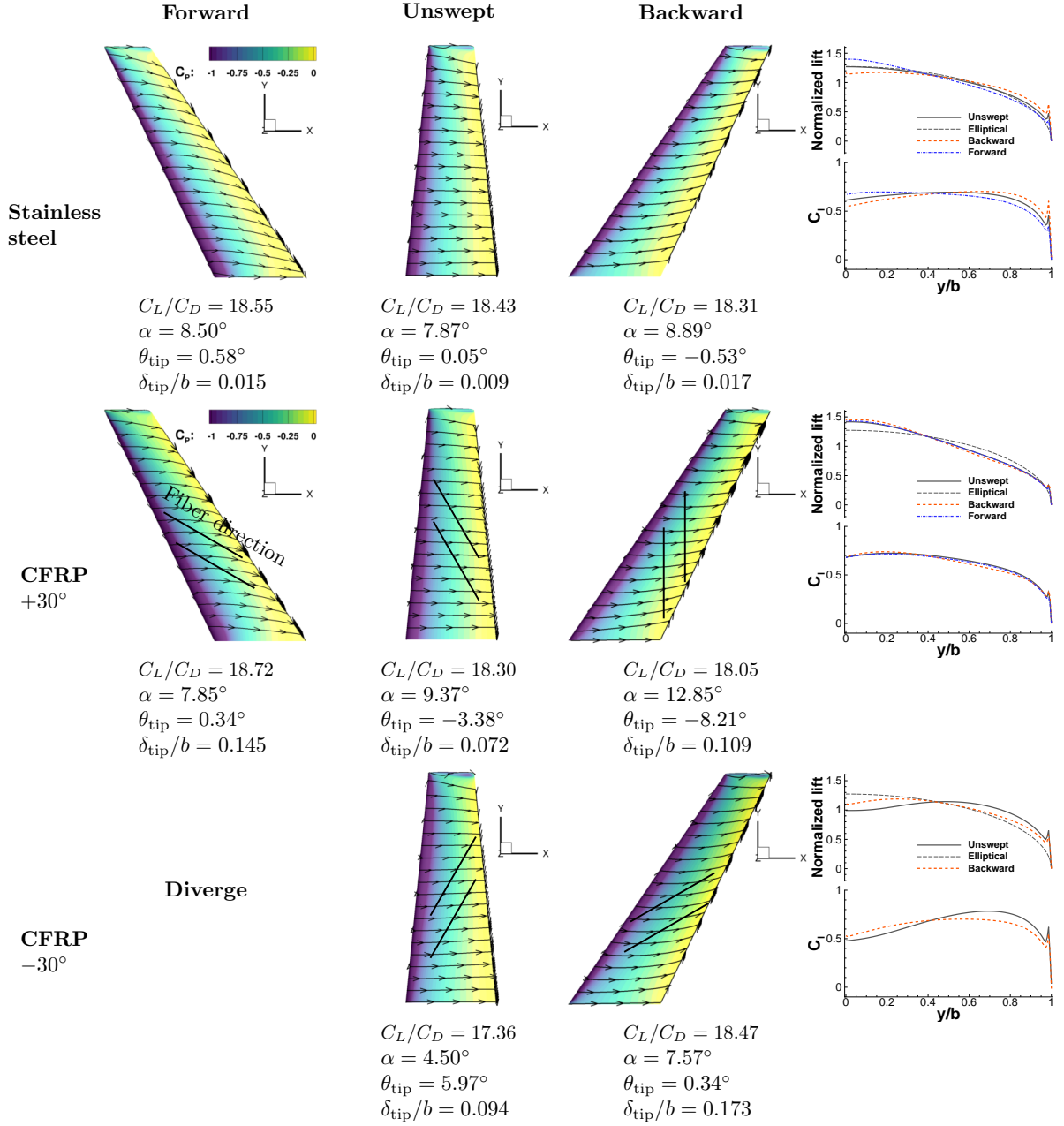


Figure 6: Hydroelastic response of different hydrofoils at  $C_L = 0.65$ , showing pressure contours and streamlines on the suction side. The right column shows the spanwise  $C_l$  and normalized lift distribution. The black solid lines represent the fiber direction. The forward CFRP  $-30^\circ$  hydrofoil diverges due to the excessive nose-up bend-twist coupling.



and bottom edges of the thick trailing edge (see Figure 7), which indicates a strong reverse pressure gradient that could result a von Karman vortex street with a distinct vortex shedding frequency that could result in noise and vibration issues.

On the other hand, swept foils exhibit reduced strength and coherence of the vortices shed behind the thick foil trailing edge, as evident by the less distorted streamlines. The spanwise component of flow for the swept hydrofoils (as shown by the streamlines in Figure 6) attenuates the reverse pressure gradient on the trailing edge, keeping the flow attached. Therefore, the unswept hydrofoil has the highest form drag, while the forward hydrofoil has the lowest.

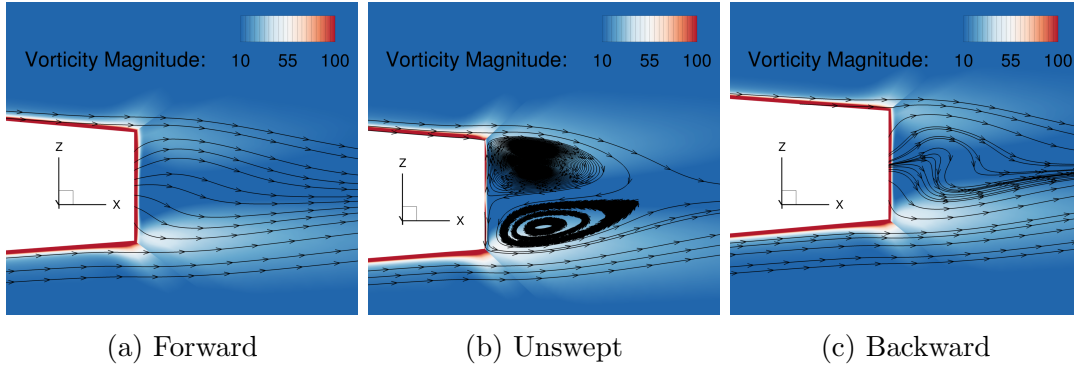


Figure 7: Streamlines downstream of trailing edge at the mid semi-span for forward, unswept, and backward stainless steel hydrofoils. Swept hydrofoils induce a spanwise flow, as observed in the streamlines shown in Figure 6, which mitigates the separation and coherent vortex structures behind the blunt foil trailing edge.

To exclude the lift-induced drag and the influence of structural displacement, we performed pure hydrodynamic simulations without structural coupling at  $C_L = 0$  to compute the zero-lift  $C_D$ . The swept forward hydrofoil has the lowest zero-lift drag coefficient ( $C_D = 0.01201$ ), while the backward hydrofoil value is a little higher ( $C_D = 0.01244$ ), and the unswept hydrofoil has the highest value ( $C_D = 0.01315$ ). In addition to form drag reduction, the trailing edge vortex suppression and incoherent structure suggests the possibility of using sweep to reduce vortex-induced vibration and noise for marine lifting surfaces, such as propellers and turbines.

In addition to changing the spanwise lift distributions, sweep also changes the deformations, as indicated by the tip deflection normalized by the semi-span ( $\delta_{\text{tip}}/b$ ) and tip twist angles ( $\theta_{\text{tip}}$ ) shown beneath the  $C_p$  contour plot for each hydrofoil in Figure 6. As illustrated by the stainless steel hydrofoils results without material-induced bend-twist coupling, sweep modified the deformations, although all these deformations are small because of the high structural stiffness.

From the modal analysis, we can see that sweep reduces the bending stiffness, so the  $\delta_{\text{tip}}/b$  of the swept hydrofoils (either forward or backward swept) are higher than that of the unswept hydrofoil. For the unswept stainless steel hydrofoil, the  $\theta_{\text{tip}}$  is positive (i.e. nose-up) because of the hydrodynamic pitching moment caused by the center of pressure being upstream of the elastic axis. In addition to the hydrodynamic pitching moment, sweep causes a geometric bend-twist coupling. As explained by Hodges and

Pierce [3, 4.2.6], when observed from the direction perpendicular to the inflow, the streamwise bending gradient results in an equivalent change in the twist measured from the global  $y$ -axis, the direction perpendicular to the inflow, as shown in Figure 8.

The geometric bend-twist coupling is nose-up for the forward stainless steel hydrofoil, which adds to the twist caused by hydrodynamic pitching moment, as evidenced by the higher  $\theta_{\text{tip}}$  value compared to the unswept case. On the other hand, the geometric bend-twist coupling is nose-down for the backward swept case, which countered the nose-up twist caused by hydrodynamic pitching moment and resulted in net negative value for  $\theta_{\text{tip}}$ . The nose-down twist near the tip also countered the higher loading near the tip caused by the induced upwash. Hence, if the loading is properly tailored, we can improve the performance of swept hydrofoils.

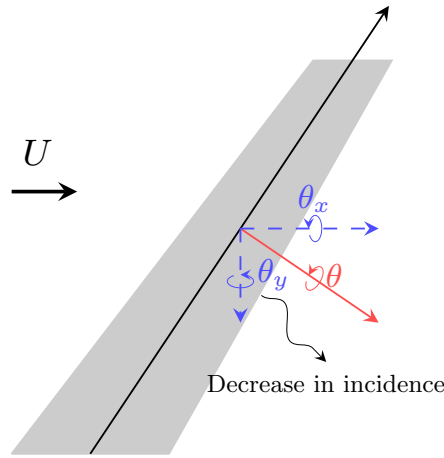


Figure 8: Sweep induced geometric bend-twist coupling.

#### 4.2.2 Coupled Influence of Sweep and Material Anisotropy

Material anisotropy can couple with sweep to change the hydrofoil deformation and thus the performance. With a positive angle of attack, positive fiber orientation (swept forward) induces a bending-up and nose-down bend-twist coupling, while negative fiber orientation (swept backward) causes a bending-up and nose-up bend-twist coupling.

The hydrodynamic pitching moment caused by the center of pressure being upstream of the elastic axis leads to a nose-up twist for all investigated hydrofoils here. As shown in Figure 6, for the unswept CFRP  $+30^\circ$  hydrofoil, the nose-down material bend-twist coupling overcomes the nose-up twist caused by the hydrodynamic pitching moment, leading to net negative  $\theta_{\text{tip}}$ , which decreases the effective incidence, and hence requires a higher  $\alpha$  to achieve  $C_L = 0.65$  compared to the unswept stainless steel hydrofoil. The unswept CFRP  $-30^\circ$  hydrofoil exhibits the opposite trend, since both the twist caused by the hydrodynamic pitching moment and material bend-twist couplings are nose-up, and hence the required  $\alpha$  to achieve  $C_L = 0.65$  is lower than the unswept stainless steel hydrofoil. Therefore, given the same geometric configuration (the same

sweep angle), the CFRP +30° hydrofoils have the lowest  $\theta_{\text{tip}}$  value compared to the stainless steel and CFRP -30° hydrofoils.

Since both forward sweep and negative fiber orientation contribute to the nose-up twist when the hydrofoil bends up, the simulations for the forward CFRP -30° hydrofoil diverged due to the excessive nose-up bend-twist coupling, and hence a rapid increase in the tip twist. This leads to early stall and flow-induced vibrations. Another extreme case is the backward CFRP +30° hydrofoil, for which the twist is the most negative ( $\theta_{\text{tip}} = -8.21^\circ$ ), and the required  $\alpha$  to achieve the target lift is the highest among all the cases investigated (12.85°).

### 4.3 Hydroelastic Performance Trends, Separation, and Stall

In the previous discussion, separation does not occur at  $C_L = 0.65$  for all hydrofoils except for the diverged forward CFRP -30° hydrofoil. To further discuss the difference in trends, separation, and stall, we perform additional hydrostructural simulations with  $\alpha = 0^\circ, 6^\circ$ , and  $12^\circ$ , as well as at  $C_L = 0.2, 0.3$ , and  $0.4$ . Figure 9 shows  $C_L$ ,  $C_D$ , pitch moment coefficient  $C_M$ , non-dimensionalized tip bending  $\delta_{\text{tip}}/b$ , and  $\theta_{\text{tip}}$ . The  $C_M$  is calculated about the mid-chord point at the root. Separation onset is identified from the reduction in the slope of the  $C_L$  and  $C_M$  curves.

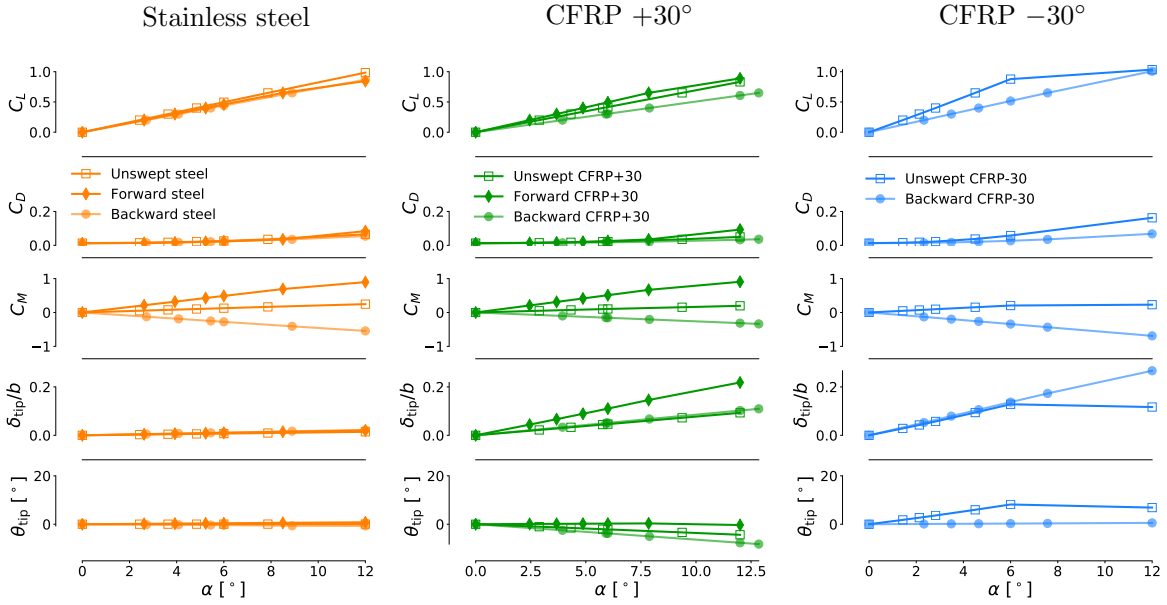


Figure 9: Force coefficients and deformations for CFRP hydrofoils with different fiber orientations and the stainless steel hydrofoils. Different combinations of sweep angle and material show different trends and separation behaviors.

For all cases investigated, the  $C_L$  increases with  $\alpha$ , but with different slopes, as shown in Figure 9. Swept hydrofoils have lower  $C_L - \alpha$  slopes, as shown in top left plot in the stainless steel results. These smaller  $C_L - \alpha$  slopes are due to the decreased effective inflow velocity compared with the unswept hydrofoil.

Although the unswept stainless steel hydrofoil has a higher  $C_L - \alpha$  slope, the swept stainless steel hydrofoils experience earlier separation, as suggested by the decreased  $C_L - \alpha$  slopes when the angle of attack increases up to  $12^\circ$ .

In the previous subsection, we showed that the sweep redistributes the spanwise loading through vorticity-induced upwash and downwash, and hence makes the lift distribution uneven and the hydrofoil becomes more susceptible to flow separation. Among the CFRP  $+30^\circ$  hydrofoils, the forward one experiences the earliest separation because the upwash near the root and the nose-down  $\theta_{\text{tip}}$  induced by material anisotropy both act to move the lift inboard, and this additional inboard load induces an earlier separation.

As the hydrofoil becomes more flexible, the effect of geometric bend-twist coupling caused by sweep affects the hydroelastic performance more strongly. Among the hydrofoils shown in Figure 9, the  $C_L$  of the unswept CFRP  $-30^\circ$  hydrofoil increases with the highest rate because the material-induced bend-twist coupling acts to induce a nose-up twist and there is no counteracting effect from geometric bend-twist coupling. This high  $C_L - \alpha$  slope also suggests an early separation and stall. The  $C_M$  of the forward and backward hydrofoils have opposite signs because the center of lift is shifted away from the middle of the root chord in different directions, which is a similar effect to that of geometric bend-twist coupling.

Using CFRP with off-axial fiber orientations decreases the bending stiffness, so CFRP  $+30^\circ$  and CFRP  $-30^\circ$  hydrofoils have higher  $\delta_{\text{tip}}$  values compared to the stainless steel hydrofoils. The  $\theta_{\text{tip}}$  shows a combined effect from the geometric bend-twist coupling, material bend-twist coupling, and hydrodynamic pitching moment. The  $\theta_{\text{tip}}$  curves of CFRP  $+30^\circ$  concentrate in the negative regime, while the curves of CFRP  $-30^\circ$  stay in the positive regime. Given the sweep angles, fiber angles, and material properties we selected, the geometric bend-twist coupling has a similar significance to the material bend-twist coupling, so the  $\theta_{\text{tip}}$  curves of the forward CFRP  $+30^\circ$  hydrofoil and the backward CFRP  $-30^\circ$  hydrofoil remain close to zero, as shown in Figure 9.

## 4.4 Efficiency and Static Divergence

To evaluate the hydrodynamic efficiency, we compare  $C_L/C_D$  over a range of lift coefficients for the hydrofoils in Figure 10. The simulations conditions are the same as in Section 4.3. As mentioned previously, the spanwise flow induced by sweep reduces the form drag, which plays a significant role in the total drag of hydrofoils with a thick trailing edge. As a result, for the stainless steel  $C_L/C_D$  curves, swept hydrofoils have higher  $C_L/C_D$  at low  $C_L$  conditions. When  $C_L$  increases to values high enough that the lift-induced drag becomes dominant, the  $C_L/C_D$  of the unswept hydrofoil approaches those of swept hydrofoils, and even outperformed the backward hydrofoil at  $C_L = 0.65$ , as shown from the stainless steel results in Figure 6.

Poor combination of composite and sweep lead to early separation and stall, which cause efficiency loss. The efficiencies of the forward stainless steel and forward CFRP  $+30^\circ$  hydrofoils drop rapidly for  $C_L > 0.65$  because of the early separation caused by the high loading near the root. The nose-up geometric bend-twist coupling caused by forward

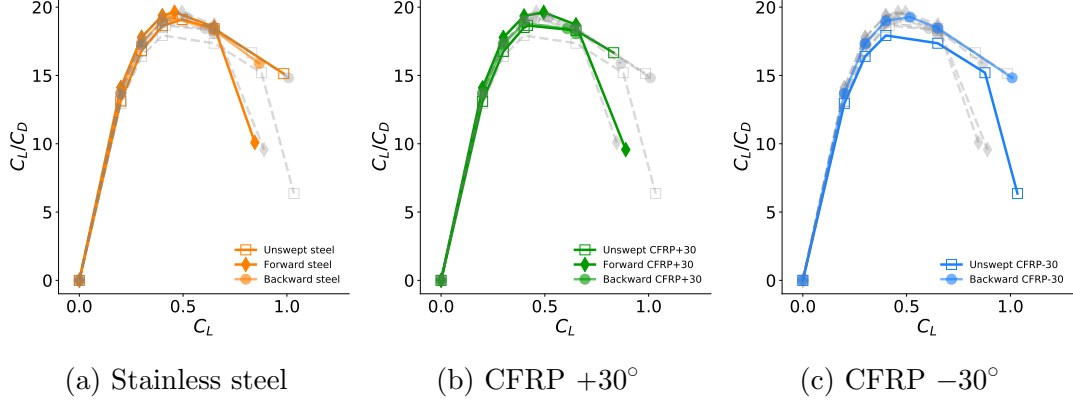


Figure 10:  $C_L/C_D$  versus  $C_L$  for all hydrofoils. Each subplot shows data of all cases. The color-highlighted solid lines correspond to the material in the title, while data of the other two material configurations are shown as gray dashed lines for comparison. Flow separation is responsible for the sudden drop in efficiency.

sweep and the nose-down material induced bend-twist coupling caused by CFRP +30° have a comparable and opposite effect, so the net twist is small (Figure 9), leading to a  $C_L/C_D$  curve and a separation behavior similar to the forward stainless steel hydrofoil. For CFRP -30°, the efficiency of the unswept hydrofoil drops at a lower  $C_L$  due to separation.

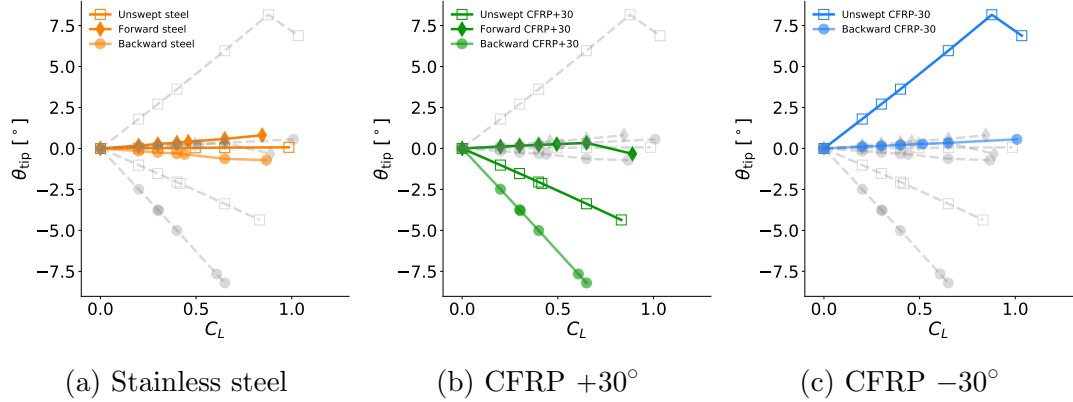


Figure 11: Tip hydroelastic twist versus lift coefficient for all hydrofoils. Nose-up bend-twist coupling increases the likelihood of static divergence. The geometric bend-twist coupling and material bend-twist coupling can counteract each other. Each subplot shows the data for all cases. The color-highlighted solid lines correspond to the material in the title, while data of the other two material configurations are shown as gray dashed lines for comparison.

Static divergence is a static instability behavior when the hydrodynamic disturbing moment is equal to or exceeds the structural elastic restoring moment. Although material failure usually happens before static divergence, it is critical to understand the static divergence behavior to avoid excessive deformation. The forward CFRP -30°

hydrofoil has an excessive nose-up bend-twist coupling, causing flow separation, and the hydrofoil is unable to generate enough restoring moment to overcome the hydrodynamic disturbing moment. Therefore, the solution diverged and a static solution cannot be obtained even at a small initial angle of attack. We assess the static divergence behaviors of the rest cases by plotting  $\theta_{\text{tip}}$  versus  $C_L$  in Figure 11. If the  $\theta_{\text{tip}}$  increases with  $C_L$ , static divergence is theoretically possible for the hydrofoil when the increasing rate or the dynamic pressure is sufficiently high. The unswept CFRP  $-30^\circ$  is expected to have the lowest static divergence speed, since  $\theta_{\text{tip}}$  increases the fastest with higher  $C_L$ , which acts to further increase the load and hence deformation. Although the backward CFRP  $+30^\circ$  hydrofoil is not susceptible to static divergence because of the nose-down twist, the twist amplitude is still so large that it can compromise the structural integrity. Therefore, designs for which  $\theta_{\text{tip}}$  decreases mildly with  $C_L$  are preferred.

## 4.5 Cavitation Inception

We have shown how the sweep changes the hydrodynamics, and how the sweep and material anisotropy interact to affect the hydroelastic response of hydrofoils. In this section, we study how the sweep and material anisotropy affect the susceptibility to cavitation. The hydrostructural solver used in this work is not capable of directly modeling cavitation, but a preliminary understanding of susceptibility to cavitation can be gained from the pressure distribution, since a low local pressure tends to encourage cavitation inception.

Since we are interested in identifying regions of low local pressure, we examine ten spanwise sections along the span and select the section with the lowest  $C_p$  for each hydrofoil, together with two sections at  $y/b = 0.2$  and  $y/b = 0.8$  as fixed references (see Figure 12). The minimum  $C_p$  values are summarized in Table. 5.

From the sectional  $C_p$  distributions of the stainless steel hydrofoils shown in Figure 12, we see that sweep makes cavitation more likely because it increases the maximum  $C_l$ , as shown on the rightmost plots in Figure 6, and therefore leads to a lower minimum  $C_p$ . However, when the material anisotropy contributes to the hydroelastic response, the spanwise loading is redistributed and the cavitation inception behavior is different from that of the stainless steel hydrofoils.

Combining the  $C_l$  plots in Figure 6 and the spanwise positions where minimum  $C_p$  occurs, we can see that the location most susceptible to cavitation is around where the maximum  $C_l$  develops. For the forward hydrofoils, the nose-down tip twist induced by CFRP  $+30^\circ$  balances the nose-up geometric bend-twist coupling and hydrodynamic pitching moment, which results in an evenly distributed loading. This reduces the suction peak, which helps the forward CFRP  $+30^\circ$  to avoid or delay cavitation compared to the forward stainless steel hydrofoil. For the unswept hydrofoil, the CFRP  $+30^\circ$  does not contribute to preventing cavitation because the  $C_l$  distribution is already even and thus there is no locally high  $C_l$  for the stainless steel hydrofoil. The nose-down tip twist and the shift of the loading towards the root makes the backward CFRP  $+30^\circ$  hydrofoil more susceptible to cavitation compared to the backward stainless steel hydrofoil. The CFRP  $-30^\circ$  helps the backward hydrofoil mitigate cavitation because the nose-down geometric bend-twist coupling is balanced by the nose-up material bend-twist coupling



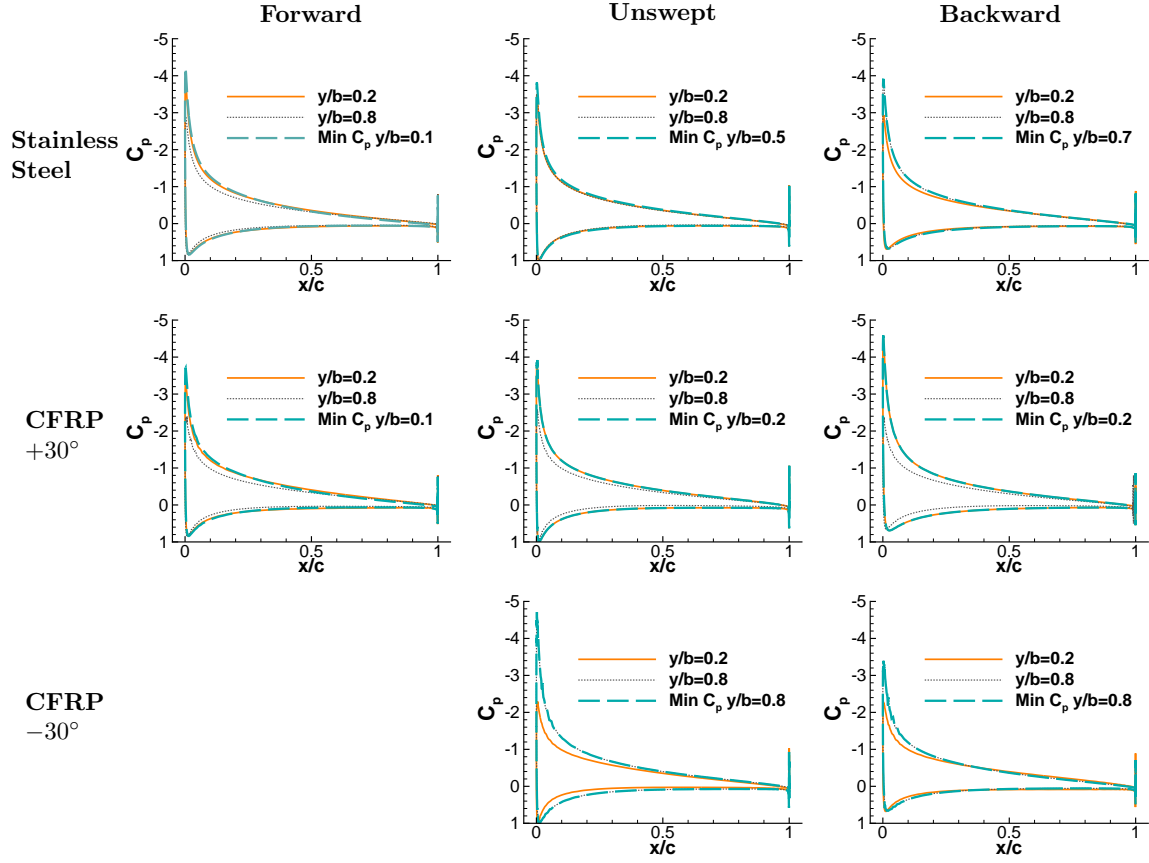


Figure 12: Sectional  $C_p$  for all hydrofoils at  $C_L = 0.65$ . The sections with the lowest  $C_p$  are shown together with the sections at  $y/b = 0.2$  and  $y/b = 0.8$ . The unswept CFRP  $-30^\circ$  hydrofoil is the most susceptible to cavitation.

and hydrodynamic pitching moment.

Besides the local pressure, the susceptibility to cavitation is also dependent on the ambient pressure. That being said, the minimum operation water depth for cavitation-free operation can be affected by the material and planform geometry. The cavitation number  $\sigma$  is conventionally used for characterizing the cavitation potential and represents the difference between the absolute ambient hydrostatic pressure ( $P_\infty = P_{\text{atm}} + \rho gh$ ) and the vapor pressure ( $P_v$ ):

$$\sigma = \frac{P_\infty - P_v}{0.5\rho U^2}. \quad (1)$$

When the minimum local absolute pressure  $P_{\min} = P_\infty + 0.5C_{p_{\min}}\rho U^2$  is lower than  $P_v$ , cavitation inception occurs, which is equivalent to

$$\sigma \leq -C_{p_{\min}}. \quad (2)$$

We assume  $P_v = 2$  kPa,  $P_{\text{atm}} = 101.3$  kPa,  $\rho_f = 1000$  kg/m<sup>3</sup>,  $g = 9.8$  m/s<sup>2</sup>, a mean-chord of 0.09 m, and a forward speed of 9.6 m/s. If the hydrofoil is operated at 7 m water depth, the cavitation number is 3.64. From Table. 5, the backward CFRP  $-30^\circ$  hydrofoil is the only one that can operate without cavitation at this water depth. To operate the forward CFRP  $-30^\circ$  hydrofoil cavitation-free, the required depth is 18 m, which is substantially deeper than for the backward CFRP  $-30^\circ$  hydrofoil. However, the NACA0009 section used here is prone to cavitation, so these computed values are used simply for comparison purposes.

Table 5: Lowest  $C_p$  among selected sections for different hydrofoils. (Lower values are colored with darker red.)

	Forward	Unswept	Backward
Stainless steel	−4.21	−3.82	−3.92
CFRP $+30^\circ$	−3.71	−3.92	−4.59
CFRP $-30^\circ$	N/A	−4.71	−3.39

## 4.6 $\lambda_2$ -criterion

Vortex structure can affect the vibration, noise, cavitation, and ventilation of marine lifting surfaces. In this section, we show the  $\lambda_2$ -criterion iso-surfaces for the hydrofoils at  $C_L = 0.65$  to study how sweep, material anisotropy, and their interaction change the vortex structure.

The  $\lambda_2$  criterion determines the existence of a local pressure minimum due to vortical motion [47, 48]. This criterion is given by

$$\lambda_2(S^2 + \Omega^2) < 0, \quad (3)$$

where  $S$  is the symmetric part of the velocity tensor  $\Delta u$ , and  $\Omega$  is the asymmetric part of  $\Delta u$ .

All hydrofoils feature a prominent tip vortex, as shown in Figure 13. The different combinations of sweep and material anisotropy not only change the strength of the vortex structure, but also the extent and direction of the vortex. The CFD mesh is probably not sufficiently fine downstream of the foil trailing edge to resolve the tip vortex, but it is sufficient to illustrate the relative differences between the foils with varying sweep and fiber angle. The forward hydrofoils have a larger tip vortex diameter, while the tip vortices of the unswept and backward hydrofoils have smaller diameters. The iso-surfaces only show a constant  $\lambda_2$ , so it is hard to distinguish the difference in the strength.

To show the difference in vortex strength, we plot slices of the backward hydrofoils with 2D contours of  $\lambda_2$ . The  $\lambda_2$  contours on  $y$ - $z$  plane at the slice 0.05 m downstream from the tip trailing edge of all backward hydrofoils are shown at the bottom of Figure 13. From the rear view shown in the 2D plots of the backward hydrofoils, we see that the tip vortex of stainless steel, CFRP +30°, and CFRP -30° propagate downstream in slightly different directions. Comparing the 2D contours, the backward stainless steel and CFRP -30° hydrofoil have tip vortices with similar strengths due to the balance of backward sweep induced nose-down bend-twist coupling and CFRP -30° induced nose-up bend-twist coupling, and both vortices are stronger than the CFRP +30° case, as indicated by the lower  $\lambda_2$  contour values inside the vortex cores. Extremely low pressure can occur in the core of a strong tip vortex, which suggests the potential for tip vortex cavitation. Additionally, pressure fluctuations in the tip vortex can cause vibration and surface erosion issues on the structures downstream.

## 4.7 Material Failure

In addition to the steady-state hydroelastic response, it is important to consider the structural integrity of the designs. First, we show how the sweep affects the structural failure by comparing the non-dimensionalized von Mises stress results for the stainless hydrofoils with different sweep angles. Second, we compare the matrix compressive/tensile cracking index contours of CFRP hydrofoils with different  $\theta_f$  and  $\lambda$  to investigate the coupled influence of sweep and material anisotropy on material failures. Since the matrix cracking failure is more likely to happen in tension, it is more important to check the tension side, which is the pressure side of the hydrofoil. Therefore, we show the hydrofoil undersides to show the side in tension. The stainless steel hydrofoils are also shown with the pressure side to be consistent.

### 4.7.1 Influence of Sweep

As discussed in Section 4.1, sweep reduces the bending stiffness, which leads to higher bending deformations for the swept hydrofoils compared to the unswept hydrofoil when subject to the same lift, as shown in Figure 14. The unswept hydrofoil has the highest non-dimensionalized von Mises stress at the maximum thickness location at the root, since the bending moment is the largest at the root for a cantilevered structure and the maximum bending stress occurs at the point that is the farthest from the midplane. For the forward hydrofoil, the combination of positive  $\theta_{\text{tip}}$  and  $\delta_{\text{tip}}$  results in a higher total bending deformation near the leading edge compared to the downstream portion.

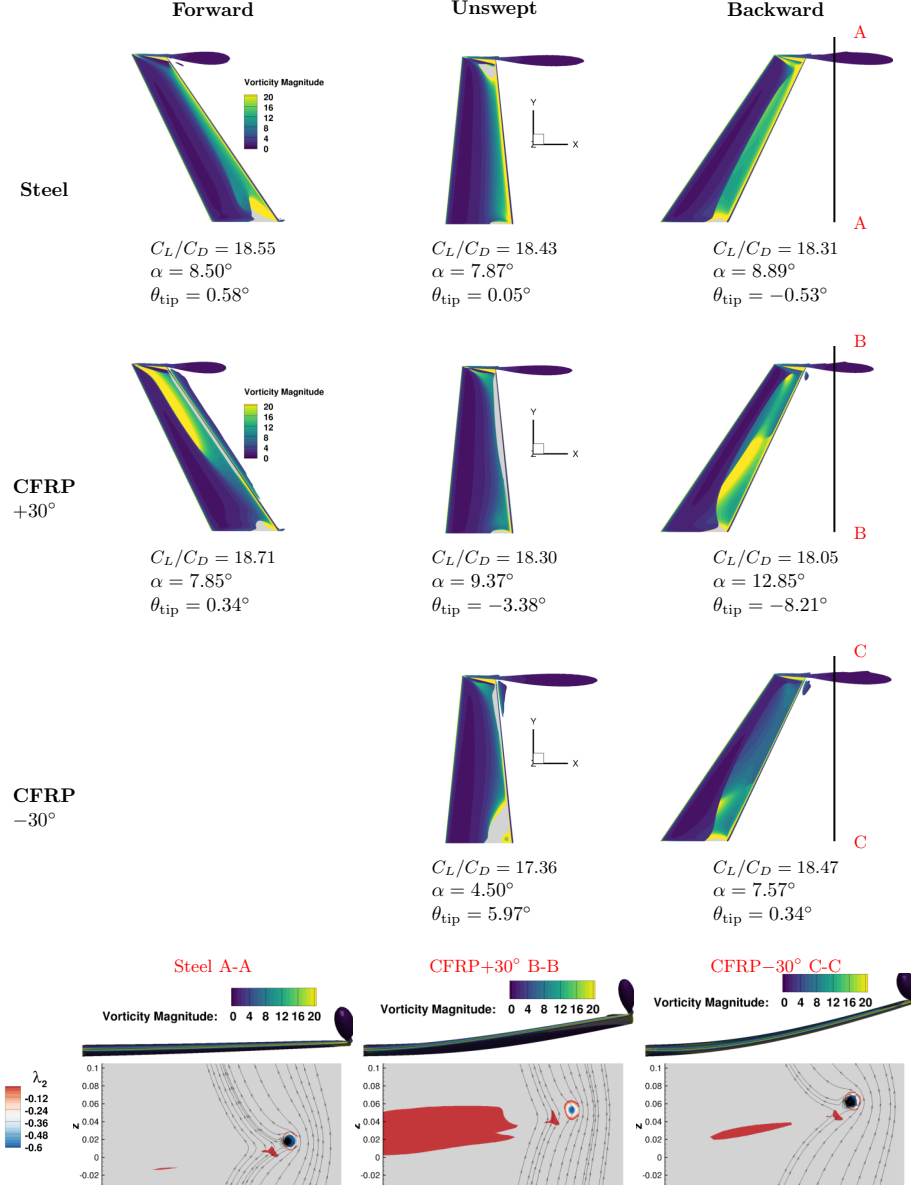


Figure 13: Iso-surfaces of  $\lambda_2$ -criterion at  $\lambda_2=-0.01$ , for different hydrofoils at  $C_L = 0.65$ . The contours on the iso-surfaces represent the vorticity magnitude. Bottom:  $\lambda_2$  contours in the  $y$ - $z$  plane at slice 0.05 m downstream from the tip trailing edge of three backward hydrofoils. Backward stainless steel and CFRP  $-30^\circ$  hydrofoils have stronger tip vortices compared to the CFRP  $+30^\circ$  hydrofoil.

As a result, the stress concentration deviates towards the leading edge for the forward hydrofoil; the opposite trend is observed for the backward hydrofoil.

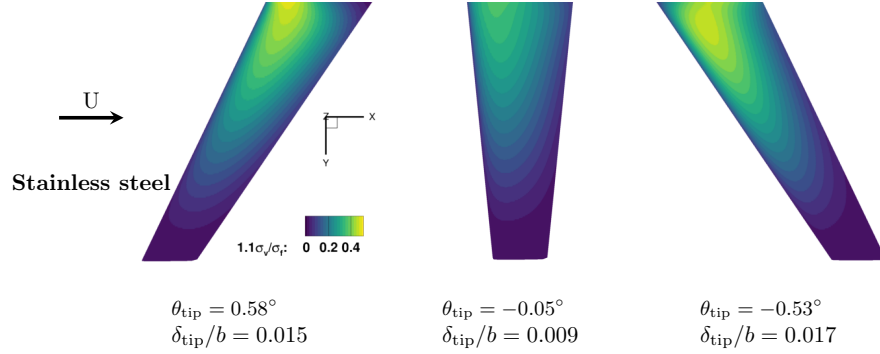


Figure 14: Non-dimensionalized von Mises stress distributions on the pressure side of stainless steel hydrofoils at  $C_L = 0.65$ . The combined deformation from bending and twisting determines the structural failure susceptibility and failure locations.

#### 4.7.2 Coupled Influence of Sweep and Material Anisotropy on Matrix Failure Inception

Composite structures have complicated failure mechanisms. The matrix inside a composite is weak and can contribute to the initiation of the material failure. Here, we use the matrix compressive/tensile cracking criterion to evaluate the material failure susceptibility and identify the failure location. The criterion is defined as,

$$I_M = \left( \frac{\sigma_{11}}{X_T} \right)^2 + \left( \frac{\sigma_{12}}{S_{12}} \right)^2 + \left( \frac{\sigma_{13}}{S_{13}} \right)^2, \text{ when } \sigma_{11} > 0 \quad (4)$$

$$I_M = \left( \frac{\sigma_{11}}{X_C} \right)^2 + \left( \frac{\sigma_{12}}{S_{12}} \right)^2 + \left( \frac{\sigma_{13}}{S_{13}} \right)^2, \text{ when } \sigma_{11} < 0 \quad (5)$$

The matrix compressive/tensile cracking failure index contours are shown in Figure 15. Both sweep and fiber orientation change failure inception and the failure location. As shown in Equations (4) and (5), since the material properties used correspond to uni-directional CFRP, the matrix cracking failure is strongly dependent on the normal stress in the direction transverse to the fiber. As a result, the effect of the fiber orientation on the material failure is not only shown by the resultant deformation but also by the stress transformation from the global coordinate to the local coordinate.

The backward CFRP  $+30^\circ$  and the unswept CFRP  $+30$  are less susceptible to matrix cracking, as shown in Figure 15. The former backward case is because most of the bending stresses can be taken by the fiber, so only a small portion is in the direction transverse to fibers after the transformation, while the latter unswept case is due to a low structural deformation. On the other hand, the forward CFRP  $+30^\circ$  and backward CFRP  $-30^\circ$  hydrofoils have larger deformations and higher normal stresses in the transverse direction because the fiber direction is less aligned with the bending stress direction, so these two hydrofoils have higher matrix compressive/tensile cracking

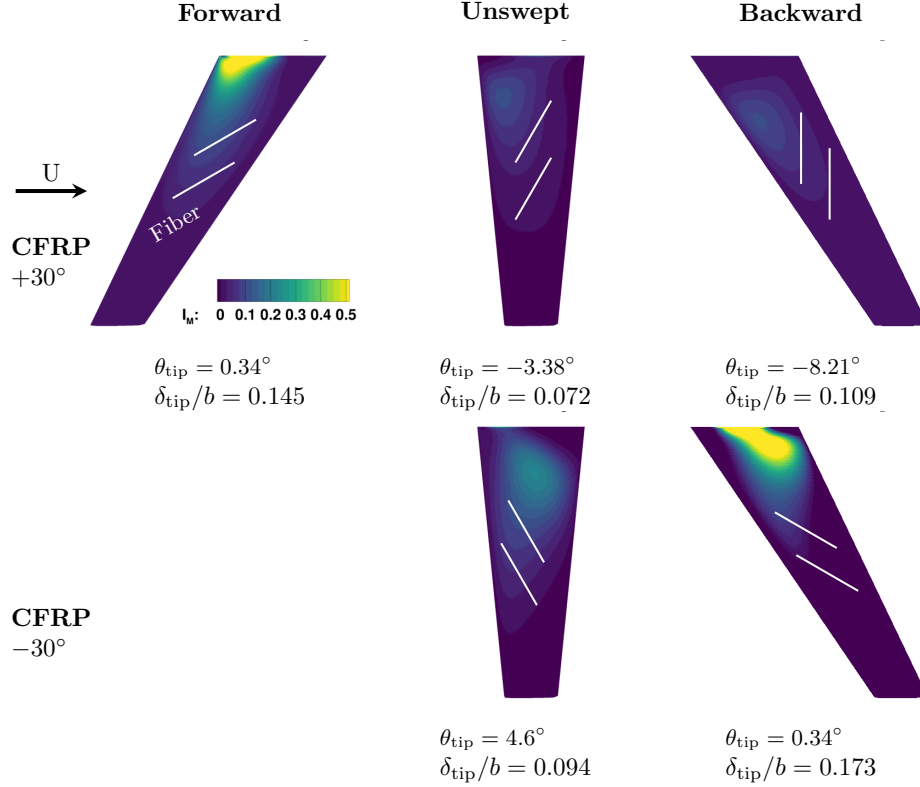


Figure 15: Matrix tensile cracking index contour of composite hydrofoils at  $C_L = 0.65$ . The results are from steady-state hydrostructural simulation. White lines represent the fiber directions. Contours are shown for the pressure side, which is the side in tension. The combined deformation from bending and twisting determines the structural failure susceptibility and failure locations. Since uni-directional CFRP is used in simulations and matrix compressive/tensile cracking is considered, the material failure is governed by the relative direction between the fiber orientation and the normal bending stress due to the poor strength in the direction transverse to fibers.



index values. The location of failure depends on the deformation and the fiber direction. All regions susceptible to material failure are perpendicular to the fiber directions, in which large deformation developed due to a lower stiffness and failure is more likely to happen due to a lower strength compared to along the fiber direction.

## 5 Conclusions

In this paper, we investigate the influence of sweep and material anisotropy on hydrofoils using a set of parametric studies comparing the natural frequencies, mode shapes, hydroelastic response (lift, drag, and moment coefficients, as well as deformation patterns), separation, stall, hydrodynamic efficiency, susceptibility to cavitation, vortex structure, and material failure.

All hydrofoils undergo bending towards the suction side due to lift. For unswept hydrofoils, the hydrodynamic pitching moment leads to a nose-up twist because the center of pressure is upstream of the elastic axis. Sweep decreases the bending rigidity due to the extended structural span, and moves the spanwise axis away from the rotation axis, which results in geometric bend-twist coupling. Forward sweep leads to a nose-up geometric bend-twist coupling, while backward sweep leads to a nose-down geometric bend-twist coupling.

With the introduction of material anisotropy, these changes in bending rigidity and bend-twist coupling behavior become more complicated. Forward leaning fiber orientation ( $\theta_f > 0$ ) leads to bending-up and nose-down twist, while backward leaning fiber orientation ( $\theta_f < 0$ ) leads to bending-up and nose-up twist. For a given  $C_L$ , the maximum nose-down twist with the highest required  $\alpha$  was observed for the backward CFRP  $-30^\circ$  hydrofoil. Changes in structural stiffness lead to different dynamic characteristics, and changes in the mode shape affect the system resonance frequencies and damping response. The reduction in bending stiffness due to the extended structural span or off-axis fiber layup challenges the structural safety, since dynamic amplification or other instabilities might occur.

Sweep changes the spanwise lift distribution due to vorticity-induced upwash and downwash, which can increase or decrease the lift-induced drag based on the actual profile. Both forward and backward sweep reduce the form drag compared to the unswept hydrofoils due to the spanwise flow that acts to reduce the strength and coherent structure of the vortices shed from the suction and pressure sides of the thick foil trailing edge. This mitigates separation, flow-induced vibration, and noise.

In addition to the hydrodynamic effects caused by the induced downwash and upwash of a swept hydrofoil, the geometric and material bend-twist coupling contribute to the change in hydroelastic response. This change redistributes the loading distribution and can improve the performance. However, an unfavorable combination can cause divergence, efficiency losses, early separation and stall, cavitation, flow-induced vibrations and noise, and material failures. The forward CFRP  $-30^\circ$  hydrofoil exhibits an excessive nose-up bend-twist coupling that physically diverges.

A high tip loading also leads to a strong tip vortex, which increases the susceptibility to tip vortex cavitation and to severe flow-induced vibration and noise.

As shown by the modal analysis, the bending rigidity of a swept hydrofoil is lower than the unswept hydrofoil. The extended span of swept hydrofoils can also increase the bending moment when subject to fluid external forces. Hydrostructural simulations of stainless steel hydrofoils with different sweeps show that the forward and backward swept hydrofoils are subject to higher stresses at the root relative to the unswept one. The geometric bend-twist effect of sweep can vary the stress concentration location, depending on the sweep direction.

Due to the anisotropic behavior of composite materials, the material failure has a fiber-direction dependency. If the hydrofoil is loaded in a way such that a significant portion of the stresses are transverse to the reinforced direction, material failure occurs at a lower loading. Therefore, strategic material design is required not only based on the optimal hydroelastic response, but must also be based on adequate structural safety to avoid material failure.

The sweep angles and fiber angles investigated in this paper are not optimized. We chose these combinations of parameters to illustrate the geometric and material bend-twist coupling effects. In a real design, if a specific sweep configuration is required to achieve certain functions, material anisotropy can help to redistribute the loading to reduce the drag and improve the efficiency. The selection of sweep, material and fiber layup should be decided together with other design variables based on high-fidelity hydrostructural optimization to ensure maximum hydrodynamic performance while avoiding cavitation, flow-induced vibration, and noise, as well as ensuring structural stability and safety. It is challenging to consider all the coupled effects and tradeoffs when a large number of variables are involved with a conventional design method because the interactions might not be intuitive, which highlights the benefit of numerical design optimization. Using low-fidelity tools can defeat this benefit of numerical optimization, as it is important to consider viscous effects and the susceptibility to material and instability failure. Therefore, there is a strong motivation to conduct high-fidelity design optimization based on the hydrostructural models with a large number of geometric and material design variables.

## 6 Acknowledgments

Support for this research was provided by the U.S. Office of Naval Research (Contract N00014-16-1-2972 and N00014-18-1-2333), managed by Ms. Kelly Cooper. The authors would like to thank Ping He and Yayun Shi for their help with the CFD mesh generation.

## References

- [1] Young, Y. L., Motley, M. R., Barber, R., Chae, E. J., and Garg, N., “Adaptive Composite Marine Propulsors and Turbines: Progress and Challenges,” *Applied Mechanics Reviews*, Vol. 68, No. 6, 2016, p. 060803. doi:[10.1115/1.4034659](https://doi.org/10.1115/1.4034659).
- [2] McLean, D., *Understanding Aerodynamics: arguing from the real physics*, Wiley, West Sussex, UK, 2013.

- [3] Hodges, D. H., and Pierce, G. A., *Introduction to Structural Dynamics and Aeroelasticity*, 2<sup>nd</sup> ed., Cambridge Aerospace Series, Cambridge University Press, 2011.
- [4] Ihara, A., Watanabe, H., and Shizukuishi, S., “Experimental Research of the Effects of Sweep on Unsteady Hydrofoil Loadings in Cavitation,” *Journal of Fluids Engineering*, Vol. 111, No. 3, 1989, p. 263. doi:[10.1115/1.3243640](https://doi.org/10.1115/1.3243640).
- [5] Cumming, R. A., Morgan, W. B., and Boswell, R. J., “Highly skewed propellers,” *Annual Meeting of SNAME*, 1972.
- [6] Laberteaux, K. R., and Ceccio, S. L., “Partial cavity flows. Part 2. Cavities forming on test objects with spanwise variation,” Vol. 431, 2001, pp. 43–63. doi:[10.1017/S0022112000002937](https://doi.org/10.1017/S0022112000002937).
- [7] Mouritz, A., Gellert, E., Burchill, P., and Challis, K., “Review of advanced composite structures for naval ships and submarines,” *Composite structures*, Vol. 53, No. 1, 2001, pp. 21–42. doi:[10.1016/s0263-8223\(00\)00175-6](https://doi.org/10.1016/s0263-8223(00)00175-6).
- [8] Young, Y. L., “Fluid–structure interaction analysis of flexible composite marine propellers,” *Journal of Fluids and Structures*, Vol. 24, No. 6, 2008, pp. 799–818. doi:[10.1016/j.jfluidstructs.2007.12.010](https://doi.org/10.1016/j.jfluidstructs.2007.12.010).
- [9] Liu, Z., and Young, Y. L., “Utilization of bend–twist coupling for performance enhancement of composite marine propellers,” *Journal of Fluids and Structures*, Vol. 25, No. 6, 2009, pp. 1102–1116. doi:[10.1016/j.jfluidstructs.2009.04.005](https://doi.org/10.1016/j.jfluidstructs.2009.04.005).
- [10] Motley, M., Liu, Z., and Young, Y., “Utilizing fluid–structure interactions to improve energy efficiency of composite marine propellers in spatially varying wake,” *Composite Structures*, Vol. 90, No. 3, 2009, pp. 304–313. doi:[10.1016/j.compstruct.2009.03.011](https://doi.org/10.1016/j.compstruct.2009.03.011).
- [11] Shirk, M. H., Hertz, T. J., and Weisshaar, T. A., “Aeroelastic tailoring — Theory, practice, and promise,” *Journal of Aircraft*, Vol. 23, No. 1, 1986, pp. 6–18. doi:[10.2514/3.45260](https://doi.org/10.2514/3.45260).
- [12] Blair, M., and Weisshaar, T. A., “Swept composite wing aeroelastic divergence experiments,” *Journal of Aircraft*, Vol. 19, No. 11, 1982, pp. 1019–1024. doi:[10.2514/3.44806](https://doi.org/10.2514/3.44806).
- [13] Lottati, I., “Flutter and divergence aeroelastic characteristics for composite forward swept cantilevered wing,” *Journal of Aircraft*, Vol. 22, No. 11, 1985, pp. 1001–1007. doi:[10.2514/3.45238](https://doi.org/10.2514/3.45238).
- [14] Weisshaar, T. A., “Aeroelastic Stability and Performance Characteristics of Aircraft with Advanced Composite Sweptforward Wing Structures,” Tech. rep., AFFDL, 1978.
- [15] Weisshaar, T. A., “Aeroelastic Tailoring of Forward Swept Composite Wings,” *Journal of Aircraft*, Vol. 18, No. 8, 1981, pp. 669–676. doi:[10.2514/3.57542](https://doi.org/10.2514/3.57542).

- [16] Young, Y. L., Yoon, H., Wright, T., and Harwood, C., “The Effect of Waves and Ventilation on the Dynamic Response of a Surface-Piercing Hydrofoil,” *32nd Symposium on Naval Hydrodynamics*, Hamburg, Germany, 2018.
- [17] Harwood, C. M., Young, Y. L., and Ceccio, S. L., “Ventilated cavities on a surface-piercing hydrofoil at moderate Froude numbers: cavity formation, elimination and stability,” *Journal of Fluid Mechanics*, Vol. 800, 2016, pp. 5–56. doi:[10.1017/jfm.2016.373](https://doi.org/10.1017/jfm.2016.373).
- [18] Harwood, C. M., Felli, M., Falchi, M., Garg, N., Ceccio, S. L., , and Young, Y. L., “The Hydroelastic Response of a Surface-piercing Hydrofoil in Multiphase Flows: Part I - Passive Hydroelasticity,” *Journal of Fluid Mechanics*, 2019. (Under review).
- [19] Harwood, C. M., Felli, M., Falchi, M., Garg, N., Ceccio, S. L., , and Young, Y. L., “The Hydroelastic Response of a Surface Piercing Hydrofoil in Multiphase Flows: Part II – Modal Parameters and Generalized Fluid Forces,” *Journal of Fluid Mechanics*, 2019. (Under review).
- [20] Harwood, C. M., Yoon, H., Young, Y. L., and Wright, T., “Dynamic Hydroelastic Response of a Surface-Piercing Strut in Waves,” *SNAME Maritime Convention*, Providence, Rhode Island, 2018.
- [21] Kramer, M. R., Liu, Z., and Young, Y. L., “Free vibration of cantilevered composite plates in air and in water,” *Composite Structures*, Vol. 95, 2013, pp. 254–263. doi:[10.1016/j.compstruct.2012.07.017](https://doi.org/10.1016/j.compstruct.2012.07.017).
- [22] Akcabay, D. T., and Young, Y. L., “Steady and Dynamic Hydroelastic Behavior of Composite Lifting Surfaces,” *Composite Structures*, Vol. 227, 2019, p. 111240. doi:[10.1016/j.compstruct.2019.111240](https://doi.org/10.1016/j.compstruct.2019.111240).
- [23] Akcabay, D. T., and Young, Y. L., “Parametric Analysis of the Dynamic Elastic Response of Composite Hydrofoils and Airfoils,” *Sixth International Symposium on Marine Propulsors, SMP’19*, Rome, Italy, 2019.
- [24] Chae, E. J., Akcabay, D. T., and Young, Y. L., “Influence of flow-induced bend–twist coupling on the natural vibration responses of flexible hydrofoils,” *Journal of Fluids and Structures*, Vol. 69, 2017, pp. 323–340. doi:[10.1016/j.jfluidstructs.2016.12.008](https://doi.org/10.1016/j.jfluidstructs.2016.12.008).
- [25] Chae, E. J., Akcabay, D. T., Lelong, A., Astolfi, J. A., and Young, Y. L., “Numerical and experimental investigation of natural flow-induced vibrations of flexible hydrofoils,” *Physics of Fluids*, Vol. 28, No. 7, 2016, p. 075102. doi:[10.1063/1.4954785](https://doi.org/10.1063/1.4954785).
- [26] Chae, E. J., Akcabay, D. T., and Young, Y. L., “Dynamic response and stability of a flapping foil in a dense and viscous fluid,” *Physics of Fluids*, Vol. 25, No. 10, 2013, p. 104106. doi:[10.1063/1.4825136](https://doi.org/10.1063/1.4825136).

- [27] Besch, P. K., and Liu, Y.-N., “Hydroelastic design of subcavitating and cavitating hydrofoil strut systems,” Tech. rep., Naval Ship Research and Development Center, Bethesda, Maryland, U.S.A., 1974.
- [28] Motley, M. R., and Young, Y. L., “Performance-based design and analysis of flexible composite propulsors,” *Journal of Fluids and Structures*, Vol. 27, No. 8, 2011, pp. 1310–1325. doi:[10.1016/j.jfluidstructs.2011.08.004](https://doi.org/10.1016/j.jfluidstructs.2011.08.004).
- [29] Liu, Z., and Young, Y. L., “Static divergence of self-twisting composite rotors,” *Journal of Fluids and Structures*, Vol. 26, No. 5, 2010, pp. 841–847. doi:[10.1016/j.jfluidstructs.2010.05.002](https://doi.org/10.1016/j.jfluidstructs.2010.05.002).
- [30] Pluciński, M. M., Young, Y. L., and Liu, Z., “Optimization of a self-twisting composite marine propeller using Genetic algorithms,” *16th International conference on composite materials, Kyoto, Japan (2007)*, 2007.
- [31] Blasques, J. P., Berggreen, C., and Andersen, P., “Hydro-elastic analysis and optimization of a composite marine propeller,” *Marine Structures*, Vol. 23, No. 1, 2010, pp. 22–38. doi:[10.1016/j.marstruc.2009.10.002](https://doi.org/10.1016/j.marstruc.2009.10.002).
- [32] Garg, N., Kenway, G. K. W., Martins, J. R. R. A., and Young, Y. L., “High-fidelity Multipoint Hydrostructural Optimization of a 3-D Hydrofoil,” *Journal of Fluids and Structures*, Vol. 71, 2017, pp. 15–39. doi:[10.1016/j.jfluidstructs.2017.02.001](https://doi.org/10.1016/j.jfluidstructs.2017.02.001).
- [33] Garg, N., Pearce, B. W., Brandner, P. A., Phillips, A. W., Martins, J. R. R. A., and Young, Y. L., “Experimental Investigation of a Hydrofoil Designed via Hydrostructural Optimization,” *Journal of Fluids and Structures*, Vol. 84, 2019, pp. 243–262. doi:[10.1016/j.jfluidstructs.2018.10.010](https://doi.org/10.1016/j.jfluidstructs.2018.10.010).
- [34] Liao, Y., Garg, N., Martins, J. R. R. A., and Young, Y. L., “Viscous Fluid Structure Interaction Response of Composite Hydrofoils,” *Composite Structures*, Vol. 212, 2019, pp. 571–585. doi:[10.1016/j.compstruct.2019.01.043](https://doi.org/10.1016/j.compstruct.2019.01.043).
- [35] Kenway, G. K. W., Kennedy, G. J., and Martins, J. R. R. A., “Scalable Parallel Approach for High-Fidelity Steady-State Aeroelastic Analysis and Derivative Computations,” *AIAA Journal*, Vol. 52, No. 5, 2014, pp. 935–951. doi:[10.2514/1.J052255](https://doi.org/10.2514/1.J052255).
- [36] Kenway, G. K. W., and Martins, J. R. R. A., “Multipoint High-Fidelity Aerostructural Optimization of a Transport Aircraft Configuration,” *Journal of Aircraft*, Vol. 51, No. 1, 2014, pp. 144–160. doi:[10.2514/1.C032150](https://doi.org/10.2514/1.C032150).
- [37] Brooks, T. R., Kenway, G. K. W., and Martins, J. R. R. A., “Benchmark Aerostructural Models for the Study of Transonic Aircraft Wings,” *AIAA Journal*, Vol. 56, No. 7, 2018, pp. 2840–2855. doi:[10.2514/1.J056603](https://doi.org/10.2514/1.J056603).
- [38] Kenway, G. K. W., Mader, C. A., He, P., and Martins, J. R. R. A., “Effective Adjoint Approaches for Computational Fluid Dynamics,” *Progress in Aerospace Sciences*, 2019. doi:[10.1016/j.paerosci.2019.05.002](https://doi.org/10.1016/j.paerosci.2019.05.002), (In press).

- [39] Mader, C. A., Martins, J. R. R. A., Alonso, J. J., and van der Weide, E., “ADjoint: An Approach for the Rapid Development of Discrete Adjoint Solvers,” *AIAA Journal*, Vol. 46, No. 4, 2008, pp. 863–873. doi:[10.2514/1.29123](https://doi.org/10.2514/1.29123).
- [40] Yildirim, A., Kenway, G. K. W., Mader, C. A., and Martins, J. R. R. A., “A Jacobian-free approximate Newton–Krylov startup strategy for RANS simulations,” *Journal of Computational Physics*, Vol. 397, 2019, p. 108741. doi:[10.1016/j.jcp.2019.06.018](https://doi.org/10.1016/j.jcp.2019.06.018).
- [41] Kennedy, G. J., and Martins, J. R. R. A., “A Parallel Finite-Element Framework for Large-Scale Gradient-Based Design Optimization of High-Performance Structures,” *Finite Elements in Analysis and Design*, Vol. 87, 2014, pp. 56–73. doi:[10.1016/j.finel.2014.04.011](https://doi.org/10.1016/j.finel.2014.04.011).
- [42] Brown, S. A., “Displacement Extrapolation for CFD+CSM Aeroelastic Analysis,” *Proceedings of the 35th AIAA Aerospace Sciences Meeting*, Reno, NV, 1997. AIAA 1997-1090.
- [43] Uyttersprot, L., “Inverse Distance Weighting Mesh Deformation,” Ph.D. thesis, Delft University of Technology, 2014.
- [44] Zarruk, G., Brandner, P., Pearce, B., and Phillips, A. W., “Experimental study of the steady fluid-structure interaction of flexible hydrofoils,” *Journal of Fluids and Structure*, Vol. 51, 2014, pp. 326–343. doi:[10.1016/j.jfluidstructs.2014.09.009](https://doi.org/10.1016/j.jfluidstructs.2014.09.009).
- [45] Phillips, A., Cairns, R., Davis, C., Norman, P., Brandner, P., Pearce, B., and Young, Y. L., “Effect of material design parameters on the forced vibration response of composite hydrofoils in air and in water,” *Fifth International Symposium on Marine Propulsors*, Espoo, Finland, 2017.
- [46] Howe, D., *Aircraft Loading and Structural Layout*, AIAA, 2004.
- [47] Jeong, J., and Hussain, F., “On the identification of a vortex,” *Journal of Fluid Mechanics*, Vol. 285, 1995, pp. 69–94. doi:[10.1017/S0022112095000462](https://doi.org/10.1017/S0022112095000462).
- [48] Felli, M., Falchi, M., and Dubbioso, G., “Hydrodynamic and hydroacoustic analysis of a marine propeller wake by TOMO-PIV,” *Fourth International Symposium on Marine Propulsors*, Austin, Texas, 2015.